Engineering Structures 307 (2024) 117885

Contents lists available at ScienceDirect

Engineering Structures

journal homepage: www.elsevier.com/locate/engstruct

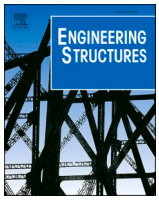

Behaviour of short columns made with conventional or FRP-confined rubberised concrete: An experimental and numerical investigation

Imad El Khouri [a], Reyes Garcia [b,*], Petru Mihai [c], Mihai Budescu [c], Nicolae Taranu [c,d], Ionut Ovidiu Toma [c], Maurizio Guadagnini [a], David Escolano-Margarit [e], Ioana Sorina Entuc [c], Gabriel Oprisan [c], Iman Hajirasouliha [a], Kypros Pilakoutas [a]

[a] Dept. of Civil and Structural Engineering, The University of Sheffield, UK
[b] Civil Engineering Stream, School of Engineering, The University of Warwick, UK
[c] Faculty of Civil Engineering and Building Services, Technical University "Gheorghe Asachi", Iasi, Romania
[d] The Academy of Romanian Scientists, Bucarest, Romania
[e] Depto. de Mecánica de Estructuras e Ingeniería Hidráulica, University of Granada, Granada, Spain

ARTICLE INFO

Keywords:
Short columns
Confined rubberised concrete
FRP confinement
Shear behaviour
Numerical analysis

ABSTRACT

Failure of short columns in concrete buildings has been extensively reported during past earthquakes. Assessing the behaviour of short columns is challenging and often requires using time-consuming advanced numerical modelling. This article presents a new and practical Short Column Macro Element (SCME) that predicts accurately the behaviour of concrete short columns. A 1/3-scale one-storey building with short columns is subjected to lateral loading tests until failure. The experimental results from the building are then used to calibrate a numerical model in Abaqus®. It is shown that the numerical model matches well the experimental results. The experimental crack patterns and stress distribution from Abaqus® are then used to determine the load path within the short column. Based on these data, a new strut-and-tie SCME is proposed and implemented in OpenSees software to simulate accurately (within 5% accuracy) the behaviour of the short columns of the tested building. Subsequently, the frame models calibrated in OpenSees and Abaqus® are modified to examine numerically the effectiveness of highly deformable FRP-confined rubberised concrete (FRP CRuC) at increasing the deformability of short columns with different levels of FRP confinement (1, 2 or 3 layers). The numerical results show that whilst the tested building failed at a small displacement of 5.4 mm (0.43% drift ratio), the use of FRP CRuC short columns with minimal confinement (1 layer of AFRP only) increased the building's displacement by almost seven times to 37 mm (3.0% drift ratio). This also enabled more redistribution of forces to other structural members of the building. This article contributes towards the development of practical design/analysis models for short columns made of conventional concrete and FRP CRuC, which are scarce in the existing literature.

1. Introduction

Current seismic codes (e.g. ACI 318–14 [1], and Eurocode 8 [2]) aim to design reinforced concrete buildings that can meet desired performance levels in terms of ductility and energy dissipation capacity. However, these two structural properties are limited by the deformation (strain) capacity of concrete columns and connections. Although a target ductility can be achieved by confining concrete with properly detailed steel reinforcement, large amounts of lateral reinforcement (links/stirrups) are often required to increase the inherently low strain capacity of concrete in compression to acceptable values. Reinforcement congestion can complicate the construction process and therefore increase the overall costs of construction. In recent years, Rubberised Concrete (RuC) has been proven to increase the strain capacity of concrete, thus emerging as an alternative material to increase the deformability of columns. In RuC, recycled rubber aggregates from waste tyres replace a fraction of the mineral aggregates in the concrete mix. While the inclusion of rubber aggregates often reduces the compressive strength and the Young's modulus of concrete, RuC can develop higher axial strains than conventional concrete (CC) for the same level of

* Corresponding author.
E-mail address: reyes.garcia@warwick.ac.uk (R. Garcia).

https://doi.org/10.1016/j.engstruct.2024.117885
Received 18 July 2023; Received in revised form 12 February 2024; Accepted 17 March 2024
Available online 23 March 2024

applied stress. Most notable is the ability of RuC to expand laterally, up to four times more than CC [3]. This property can be exploited to increase the axial capacity and deformability of RuC through the use of external Fibre Reinforced Polymer (FRP) confinement.

Previous studies have investigated the behaviour of Confined RuC (CRuC) cylinders and columns. For instance, Youssf et al. [4] reported high axial compressive strengths (up to 112.5 MPa) in RuC cylinders confined with Carbon FRP (CFRP) jackets. However, since only 20% of rubber replaced the sand volume in their tests, the maximum axial strains (1.8%) reported by Youssf et al. were comparable to those achieved in normal FRP-confined concrete [5]. This indicates that high volumes of rubber replacement (>50–60%) are necessary to increase deformability. Likewise, Duarte et al. [6] reported a 50% increase in ductility by confining RuC columns with cold-formed steel tubes, although a lower confinement effectiveness was achieved due to the lower dilation angle of RuC [7]. More recent research [8,9] has also proven the effectiveness of Glass (GFRP) and CFRP jackets at enhancing the axial capacity and deformability of square/circular RuC elements. Past research has also shown that flexural-dominated structural elements incorporating RuC and CRuC can develop higher ductility, damping and energy dissipation capacity compared to CC counterpart elements [10–14]. Whilst most of the research to date has examined isolated structural elements, much less research has focused on the shear behaviour of buildings made of RuC or CRuC. A recent study [15] has shown that an increase of rubber replacement levels leads to a decrease in the shear strength of RuC, but also to a better post-peak softening behaviour at relatively high rubber contents (about 60% replacement). In addition, tests by the authors [16] proved that the use of a minimal external confinement (one layer of Carbon FRP (CFRP)) can enhance both the shear deformations (up to forty times) and shear strength (two times) over RuC counterparts.

In buildings located in seismic-prone areas, the geometry of structural elements and their relative stiffnesses significantly affect the load distribution paths and can limit structural performance. For instance, short columns are typical examples where the relatively high stiffness of the element can lead to catastrophic failures [17]. Short columns are columns where the shear ratio α_s is defined as $\alpha_s = \frac{M}{Vl} \leq 2.5$, where M is the end moment, V is the shear force, and l is the width of the column [18–21]. Whilst design codes advise to avoiding the use of short columns in buildings, many times these are necessary due to architectural requirements in parts of the buildings (e.g. in partially buried basements, stair and platform connections, mezzanine floors, and buildings on sloping grounds). Short columns can also be created unintentionally when non-structural partial infill walls or parapets are added between columns. The behaviour of short columns is dominated by shear and therefore (if inadequately detailed) brittle failures can occur, with limited yielding and force redistribution. If short columns are necessary, the use of construction materials able to develop high deformation and rotational capacity (such as CRuC) is expected to promote a better force redistribution and a higher energy dissipation. However, further research is needed to verify the potential of CRuC at improving the shear behaviour of short columns subjected to lateral load. Moreover, conventional seismic analysis tools based on fibre element cannot account for the shear dominated behaviour of short columns, and therefore there is also a need for the development of practical tools to analyse buildings with short columns.

This article proposes a new and practical Short Column Macro Element (SCME) that predicts accurately the behaviour of concrete short columns. The first part of the article presents lateral loading tests on a 1/3-scale one-storey concrete building with short columns. The results from the tested building were used to calibrate a finite element model in Abaqus® software, which provided a thorough insight into the structural behaviour of the short columns. The results from Abaqus® (crack patterns and stress distribution) were subsequently used to develop a new practical Short Column Macro Element (SCME) adopting a strut-and-tie approach to determine its geometry. The SCME was then implemented in OpenSees [22] to simulate the behaviour of the short columns of the tested building. Next, both frame models calibrated in OpenSees and Abaqus® were modified to examine numerically the effectiveness of highly deformable FRP CRuC at increasing the deformability of short columns with different levels of FRP confinement (1, 2 or 3 layers of FRP). This article contributes towards the development of practical design/analysis models for short columns made of conventional concrete and FRP CRuC, which in turn is expected to promote the use of CRuC in shear applications. This study is part of the EU-funded multi-partner project Anagennisi that aimed to develop new RuC and CRuC applications to reuse all tyre components in concrete [23].

2. Experimental programme

2.1. Characteristics of tested building

A one-bay one-storey 1/3 scaled-down concrete building was built and tested at the Technical University "Gheorghe Asachi" of Iasi, Romania, as part of the EU-funded project Anagennisi [24]. The scaled-down building is deemed to represent part of a typical school building, which often have one floor and one bay in one direction. Moreover, numerous school building in past earthquakes have experienced damage or collapse due to short column failures. The building had a storey height of 1360 mm, total length of 2550 mm in the direction of loading (X direction), and a width of 1950 mm in the other direction (see Fig. 1a). The primary consideration in the design of the building was to produce a local shear failure in the short columns, and therefore the column flexural capacity was higher than its shear capacity. Moreover, in order to attain a shear failure in the short columns, the beams were intentionally over strengthened, and the columns' shear reinforcement consisted of mild steel. The four columns had a cross-section of 150 × 150 mm (Fig. 1b) and an effective height of 1100 mm. The base of the columns was bigger (220 ×220 mm) and this was embedded in a rigid steel foundation for a depth of 400 mm. The rigid steel foundation was in turn bolted to the strong floor of the laboratory. The beams measured 150 × 260 mm (Fig. 1b). The columns' longitudinal reinforcement consisted of six 14 mm diameter bars, and these were bent at the ends at a 90° for anchoring. The columns' shear reinforcement consisted of closed stirrups of 4 mm diameter spaced at 100 mm centres. Stirrups were also provided in the beam-column joints. The longitudinal reinforcement of beams in the X (direction of loading) and Y directions consisted of six 12 mm and four 10 mm diameter bars, respectively. The beams had 6 mm diameter stirrups spaced at 200 mm centres in the midspan of the beam, and spaced at 100 mm centres at the ends. The longitudinal steel bars of the beams were anchored at a 90° angle. The slab had a thickness of 60 mm and it was reinforced with a mesh of 6 mm diameter bars at 100 mm centres (Fig. 1a). The clear concrete cover was 20 mm in all structural elements. It should be noted that the corners of the short columns were rounded off (radius = 25 mm) since the short columns of a twin building were to be confined with FRP jackets, and both buildings were cast at the same time.

The columns were intentionally designed to fail in shear at the top region just below the beams, where two braced steel frames (placed along axes 1 and 2) formed a short column (Fig. 1c). The columns had a theoretical flexural yield capacity of 23 kNm, an ultimate flexural capacity of 25 kNm, and a maximum shear capacity of 28 kN for the concrete alone according to Eurocode 2 (EC2) [25]. The shear stirrups of the column provided an additional 6.9 kN resistance. Therefore, at the total (theoretical) shear resistance of 34.9 kN, the bending moment of the short column was only 5.2 kNm, which was well below the flexural yield capacity of 23 kN. The ultimate flexural capacities of the longitudinal beams (X direction) and transverse beams (Y direction) were 46 and 22 kNm, respectively.

The structural elements of the building were identified based on their

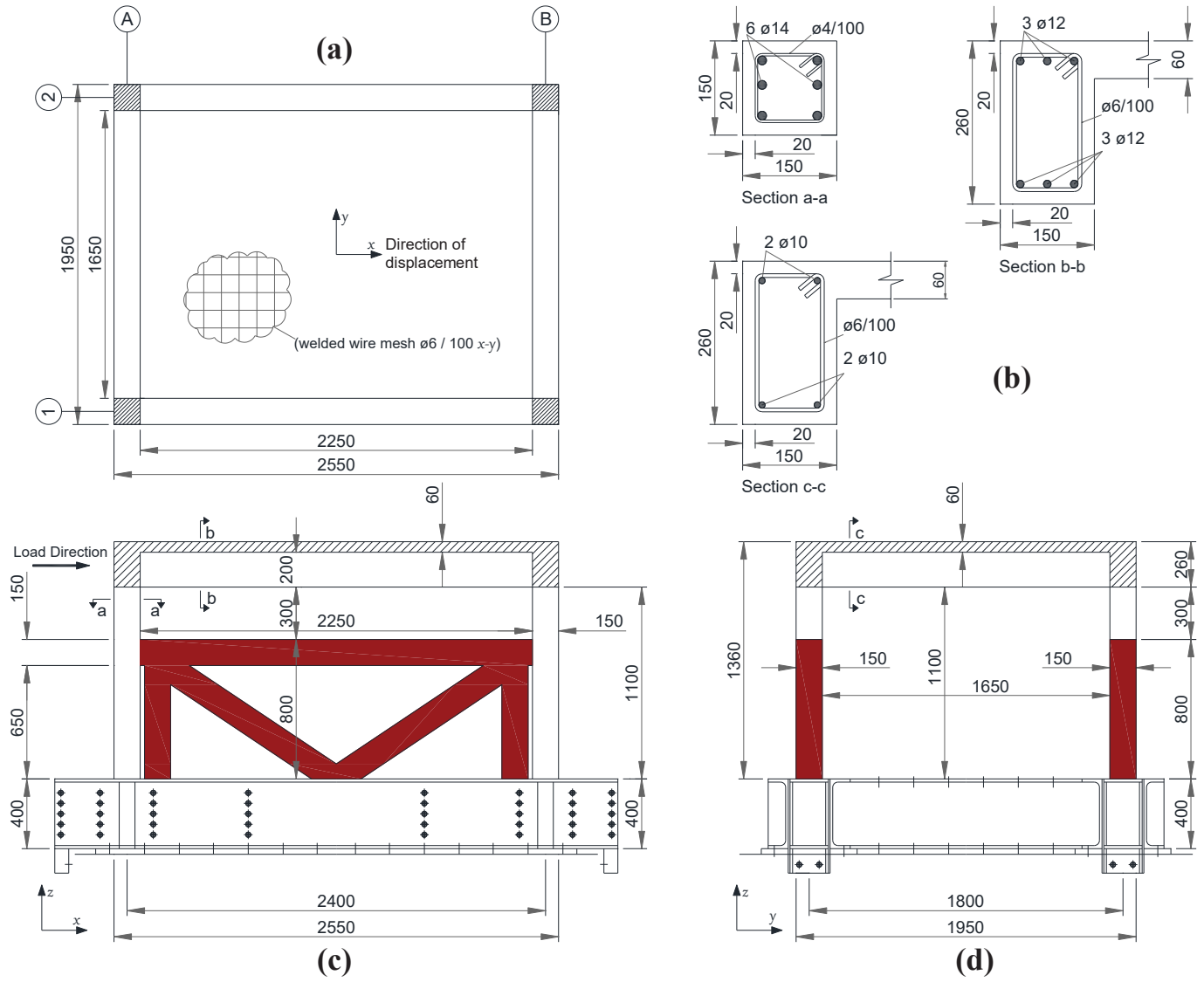

Fig. 1. Geometry and details of tested building (a) plan view, (b) cross sections of elements, (c) elevation showing loading direction and braced steel frames, and (d) elevation in transverse direction.

type, location, and orientation. The first letter of the ID indicates the type of structural element (C=column, J=beam-column joint), while the next digit and letter represent the location of the element based on the intersection of the corresponding axes shown in Fig. 1a. The fourth letter, if used, determines the direction being referred to. For example, J1A-X refers to the joint situated at the intersection of axes 1 and A, and the face being observed is parallel to the X-axis.

2.2. Material properties

A single concrete mix with water/cement ratio $w/c = 0.4$ was used to cast the building. The mechanical properties of the concrete were determined by testing five 150 × 300 mm standard cylinders according to EN 12390–3 [26], which resulted in a mean compressive strength f_{cm} = 37 MPa and a Young's modulus E_c = 30 GPa. The tensile strength of the concrete was obtained from three standard cylinders and was f_{ct} = 3.3 MPa. The longitudinal bars of beams and columns had yield and ultimate strengths of f_{ly} = 513 MPa and f_{lu} = 626 MPa, respectively. These values were obtained from five direct tensile coupons tested according to EN 10080 [27]. The smooth steel wire used for the stirrups and steel mesh of the slab had a yield strength of f_{sy} = 255 MPa, according to the producer's data.

2.3. Test setup, instrumentation, and load sequence

Two braced steel frames restrained the columns in the X-direction and simulated partial infill masonry walls. Such restraining steel frames were bolted to the bottom steel foundation and forced the development of a short column mechanism within the top region of columns C1A and C2A. The clear shear span of the short column was 300 mm, which results in a shear ratio α_s = 1. Ten concrete blocks (total = 36 kN) were bolted to the slab to simulate axial load, thus resulting in an axial load of 9 kN per column, or approximately 1% of the column's axial capacity. Such relatively low axial load was applied due to the limited availability of blocks in the laboratory. Additionally, this test was needed to inform future shake-table tests on a similar building, where the maximum overturning moment was limited to the capacity of the shake table.

The building was instrumented in the X direction with eight horizontal linear variable differential transformers (LVDTs) shown as Ln1 to Ln8 in Fig. 2. These LVDTs were located at the top and bottom of the short columns. Four diagonal LVDTs (Incl1 to Incl4 in Fig. 2) placed at an angle of 45° measured the relative rotation between beams and columns.

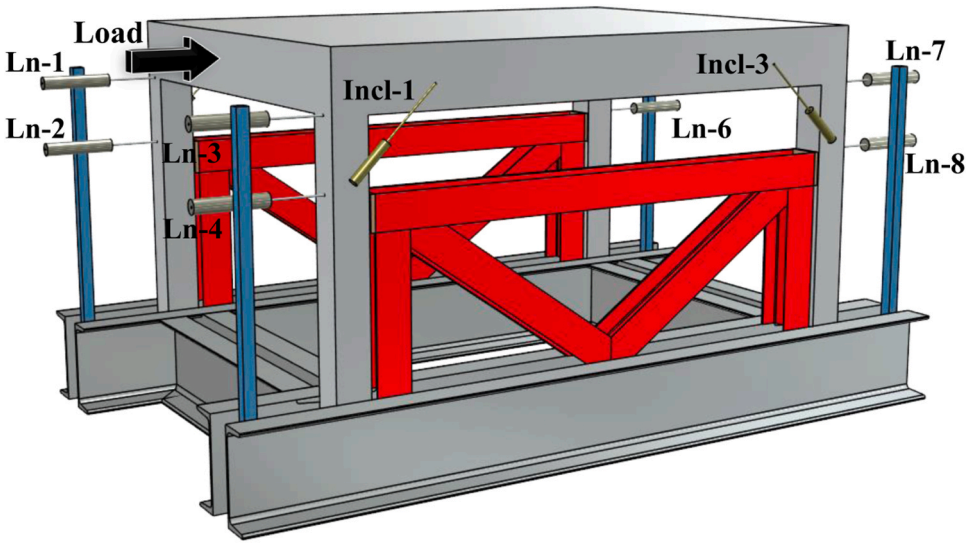

Fig. 2. Schematic view of test setup and instrumentation of tested building.

The lateral load was applied monotonically on the transverse beam via a hydraulic actuator and a stiff transfer steel plate. The test was performed in load control at a rate of 6 kN/min. The building was subjected to three sets of three cycles each: i) set 1 performed at 40 kN to capture the first flexural crack, ii) set 2 performed at 60 kN, and iii) set 3 performed at 100 kN to capture the diagonal shear cracking. This was followed by a final monotonic load up to failure of the short columns. The test was halted when the maximum load recorded during the test dropped by 20%. Fig. 3a shows the experimental model and setup. The lateral actuator applied the force directly on the building using a stiff steel plate to transfer the load (Fig. 3b).

2.4. Test results and discussion

Fig. 4 shows the lateral load vs displacement of the building. The displacements are the average of four horizontal transducers (Ln-1, 3, 5, and 7). In this figure, the top horizontal axis also shows the drift ratio of the unrestrained column (centreline height of 1230 mm).

The results in Fig. 4 indicate that the first flexural crack occurred at joints J1A and J2A during the first loading cycle (set 1) at a lateral force of 37 kN. The cracks propagated at an angle of 45° and 70° from the horizontal for J1A-X and J2A-X, respectively. The cracks further propagated through the joints during the subsequent cycles performed at 40 kN (set 1) and 60 kN (set 2). A few hairline flexural cracks appeared along columns C1A-X and C2A-X during set 3 at 100 kN. At a lateral

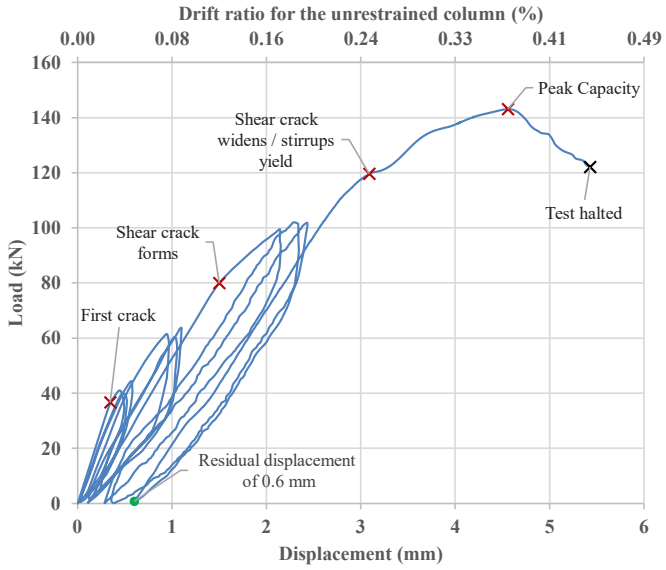

Fig. 4. Load vs displacement curve of tested building.

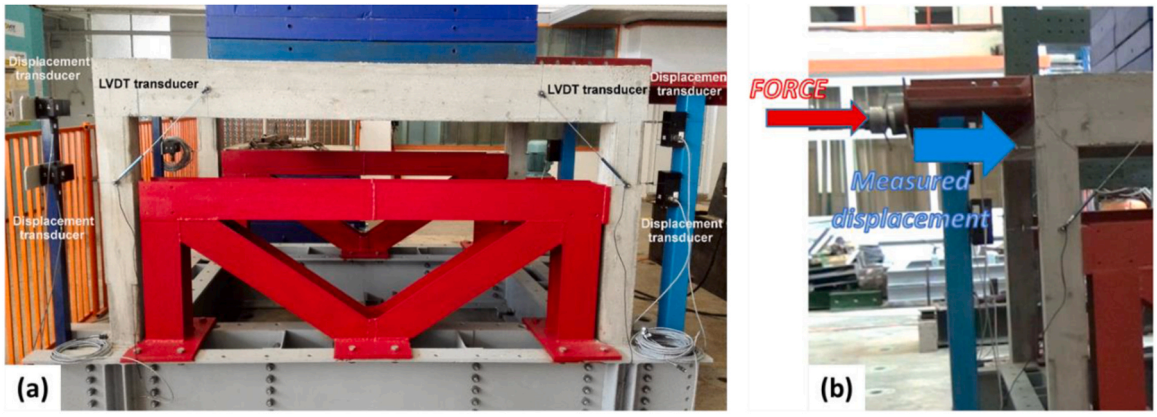

Fig. 3. (a) General test setup, and (b) actuator and stiff transfer plate to apply load.

force of 82 kN, shear cracking occurred in the top portion of both columns C1A-X and C2A-X. The shear crack propagated at an approximate angle of 17° from the vertical along the direction connecting the externally applied load to the internal restraining system as the main load transfer mechanism relied on the formation of a diagonal compression strut. Failure of the building occurred at a small displacement of 5.4 mm (0.43% drift ratio) of the unrestrained column. Figs. 5a-b show, respectively, damage experienced at the short columns and joints J1A and J2A after the test.

Flexural cracking in columns C1B-X and C2B-X initiated during the second cycle at 100 kN (set 3) at approximately 98 kN. The maximum lateral load capacity of the building (143 kN) occurred at a lateral displacement of 4.55 mm. Failure was deemed to occur at a displacement of 5.4 mm (121 kN) following excessive concrete spalling at the top of columns C1A-X and C2A-X. No damage was observed in the slab or the beams. No torsion was recorded as the displacements measured by the LVDTs were similar on both sides of the building. The initial stiffness of the building was 107 kN/mm, measured experimentally from the slope of the load-displacement data up to a load of 30 kN. The stiffness at the start of set 3 was 48 kN/mm (i.e. only 45% of the initial stiffness in set 1).

Fig. 6 shows the beam-column relative rotation at axis-A (θ_A) and axis-B (θ_B) recorded during the test. The first stiffness change (due to flexural cracking) is observed in the rotation at axis-A (marked with an ×). However, the rotation at axis-B does not show any significant stiffness change since the columns and joints at axis B only showed signs of damage at a lateral load of 98 kN. In the next section, the results from these tests are used to study in more detail the structural response and failure mode of the short columns of the building.

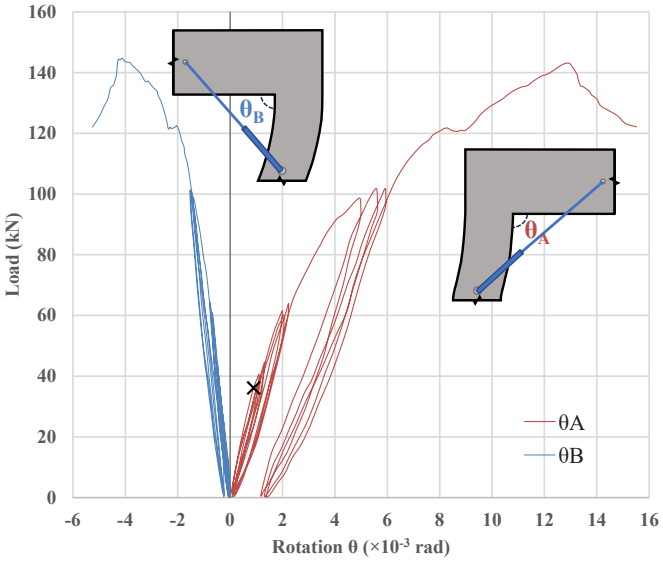

Fig. 6. Average beam-column relative rotation at axis A (joint opening) and axis B (joint closing).

3. Numerical modelling of building in Abaqus®

3.1. Geometry and loading protocol

To study in more detail the response and failure mode of the short columns, the tested building was modelled in Abaqus® [28] software. Due to symmetry and absence of in-plan torsion during the test, the building was modelled as a 2D frame. The geometry of the model

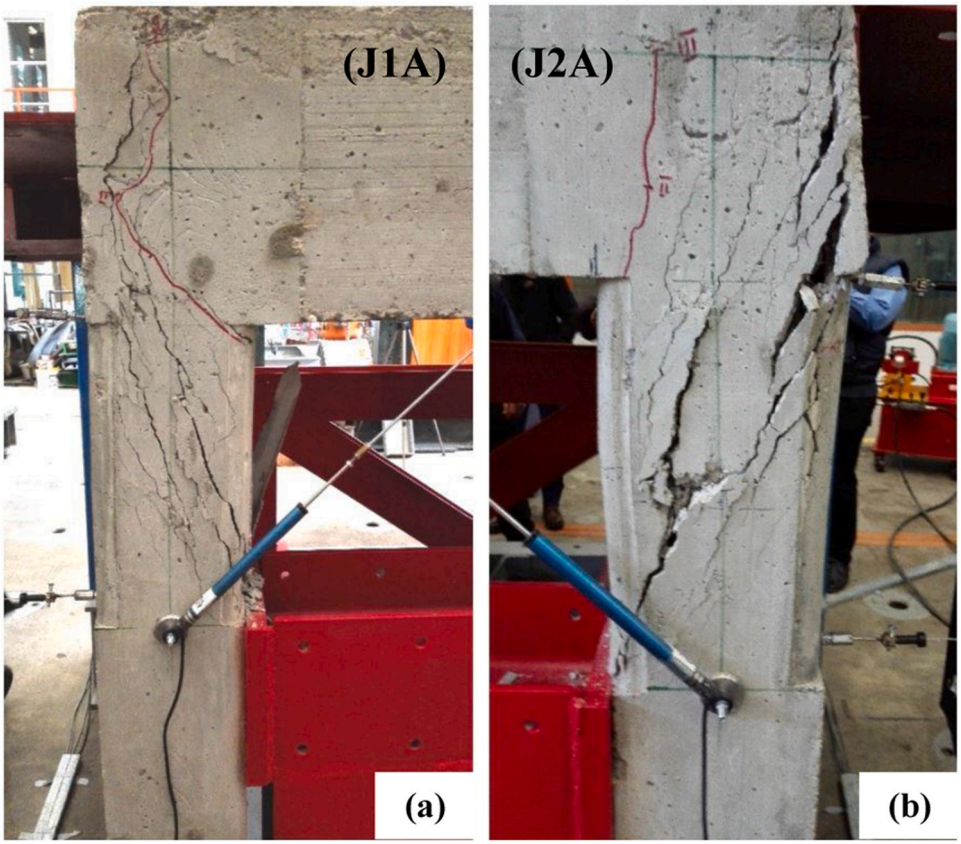

Fig. 5. Shear cracks along short columns and damage of joints (a) J1A, and (b) J2A (excessive spalling in column C2A occurred after peak capacity).

corresponds to that shown in Figs. 1a-d. The bottom 400 mm of the columns were fully restrained along the sides to simulate the fixity provided during the tests by the rigid steel foundation. The braced steel frame was modelled as a 3D analytical rigid body. The interaction between this rigid body and the concrete column was simulated by a surface-to-surface hard contact (with no friction), but allowing separation after contact. The gravity load was applied as concentrated forces on reference points (control nodes). Increasing displacements were imposed on a reference point connected to joint J1A. The reference points were connected to their corresponding transfer steel plate via a Multiple Point Constraint (MPC) tie. Abaqus/Standard was used to perform a static analysis with viscoplastic regularisation, using a viscosity parameter of value of 1E-5. The frame was pushed monotonically until failure as done in the test. The model was built in Abaqus/Standard (Implicit) using a general static analysis.

3.2. Concrete and steel reinforcement models

The built-in concrete damage plasticity model (CDP) in Abaqus/Standard was used in the analysis with the following plasticity parameters: dilation angle $\psi = 37°$; eccentricity $\epsilon = 0.1$; stress ratio $\sigma_{b0}/\sigma_{c0} = 1.16$; and shape factor of the yield surface $K_c = 0.667$. The value of the dilation angle was determined based on a sensitivity analysis (as reported by El Khouri [29]), whereas the parameters ϵ, σ_{b0}/σ_{c0}, and K_c were taken as the default values given by Abaqus®. The compressive stress-strain behaviour was defined according to the Krätzig and Pölling [30] elasto-plastic damage model, whereas the tensile softening function was defined based on the stress-crack opening relation by Hordijk [31]. The CDP damage parameters (for both compression and tension) were defined using the damage evolution model proposed by Alfarah et al. [32]. The adopted framework implements a fracture energy-based regularisation and ensures mesh-independent results. The fracture energy G_F (in N/m) of concrete was calculated using Eq. (1) [33]:

$$G_F = 2.5\alpha_0 \left(\frac{f_{cm}}{0.051}\right)^{0.46} \left(1 + \frac{d_a}{11.27}\right)^{0.22} \left(\frac{w}{c}\right)^{-0.3} \quad (1)$$

where α_0 is 1 for round aggregates; d_a is the maximum aggregate size; and w/c is the water-cement ratio by weight.

In this study, round aggregates of maximum size 15 mm were used in the concrete used to cast the tested building. Likewise, a compressive strength $f_{cm} = 37$ MPa was obtained from the tested cylinders (see Section 2.2). Adopting $\alpha_0 = 1.0$, $f_{cm} = 37$ MPa, $d_a = 15$ mm, and $w/c = 0.4$ (according to the concrete mix in Section 2.2), the fracture energy was calculated as 82 N/m. The crushing energy G_C was taken to be 100 times the fracture energy, as suggested in previous studies [34]. All the concrete parts of the model were meshed with an 8-node linear 3D brick element with reduced integration (C3D8R) as past research [35] proved that this is the most suitable element for 3D models with regular geometry.

The longitudinal steel bars and stirrups were modelled as 2-node linear 3D truss elements (T3D2) assuming an elastic-perfectly plastic behaviour. All reinforcement was fully embedded in the concrete assuming perfect bond. This is reasonable as no debonding of bars was observed during the test. The transfer steel plates used for loading were modelled as 3D solid C3D8R elements with an elastic behaviour.

3.3. Numerical results and discussion

A mesh sensitivity analysis was performed using a different number of elements (4, 5, 6 or 8) across the width of the column, thus resulting in mesh sizes of 37.5, 25, 30, and 18.75 mm, respectively. Fig. 7 compares the lateral load vs displacement results obtained for each element size, as well as the envelope of the experimental results. Whilst some minor differences can be observed in terms of both peak load and

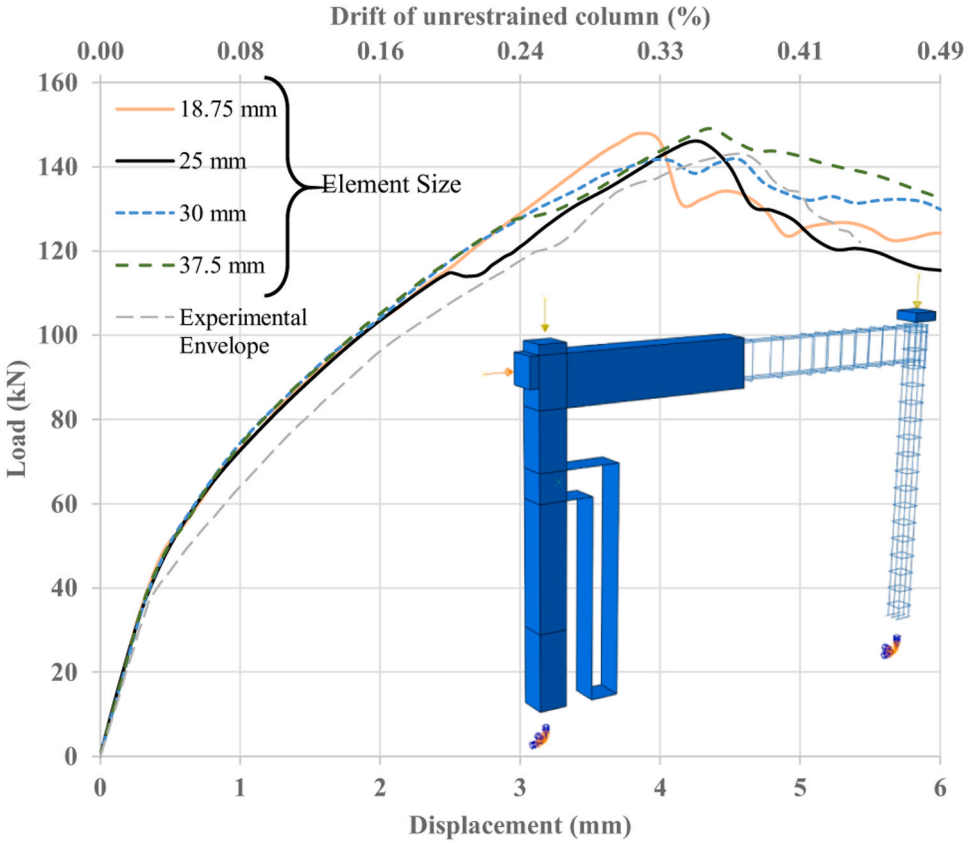

Fig. 7. Load vs displacement for mesh sensitivity analysis in Abaqus® frame model.

displacement, the initial stiffness and subsequent degradation of all models are similar regardless of the mesh size. The results from the 25 mm mesh are considered to best fit the experimental results and are discussed herein. The peak lateral capacity and displacement predicted by the model were 146 kN and 4.2 mm, respectively, which compare well with the experimental values 143 kN and 4.55 mm. The initial stiffness of the model (120 kN/mm) was 12% higher than the initial experimental stiffness (107 kN/mm). The higher stiffness of the Abaqus® model can be attributed to minor unintended cracking caused to the building while positioning it on the testing rig with a crane. At a load of 43 kN, flexural cracking occurred simultaneously in joint J1A-X and along the external face of column C1A-Y (at the level of the braced steel frame) and this is well captured by the model. However, the stiffness reduction after 43 kN was less severe than that in the test, which led to a slightly stiffer response. A sudden increase in lateral displacement was observed at 114 kN, which can be attributed to yielding of the top stirrups in column C1A just below the joint. Such increase in lateral displacement was also observed at 110–130 kN in the other models with different mesh sizes, although the displacement is much less noticeable. Moreover, it is also possible that the difference in mesh size for the same viscosity parameter adopted in the analysis could have led to minor conversion issues in the model with a 25 mm mesh. Accordingly, it is considered that yielding of the stirrups occurred in this short column. However, the longitudinal column bars remained elastic both in the test and the numerical analysis.

The minimum principal stress field along the column and the joint at a displacement of 3.75 mm (see Fig. 8) shows the compressive force path within the short column. The results show that the analytical stress distribution agreed very well with the experimental cracking pattern. Consequently, the 2D frame model in Abaqus® can provide details of the evolution of the main load transfer mechanism within the short columns. Based on the experimental evidence and numerical results, it is possible to conclude that a diagonal concrete strut connecting the bottom of the beam at the loading side to the top of the braced frame clearly formed at a displacement of about 1.2 mm. The dimensions of the nodes of such strut were estimated from the numerical model to be 65 mm and 45 mm for the top and bottom nodes, respectively. These dimensions, which agree well with cross-section analysis calculations, defined the geometry of nodes and strut used to develop the new model proposed in the following section.

4. New Short Column Macro Element (SCME) and OpenSees analysis

Whilst the finite element model of the building (Section 3) matched well the experimental results, such type of analysis is computationally demanding and therefore somehow inconvenient to analyse large buildings and/or dynamic loading effects. Consequently, this section presents a new and practical analytical model to analyse buildings with short columns. The model is implemented in OpenSees [22] software for comparisons with the finite element model.

4.1. Frame geometry and element type

The tested building was modelled as a single 2D frame made of displacement type beam-column elements. The cross-section of the elements was discretised with fibres of three materials (see Fig. 9a): i) unconfined concrete (concrete cover), ii) confined concrete (core concrete) modelled based on Chang and Mander's confinement model [36], and iii) steel (reinforcing bars). Six strut and tie elements (Fig. 9a) were used to model the shear load-transfer mechanism within the short column, as detailed below.

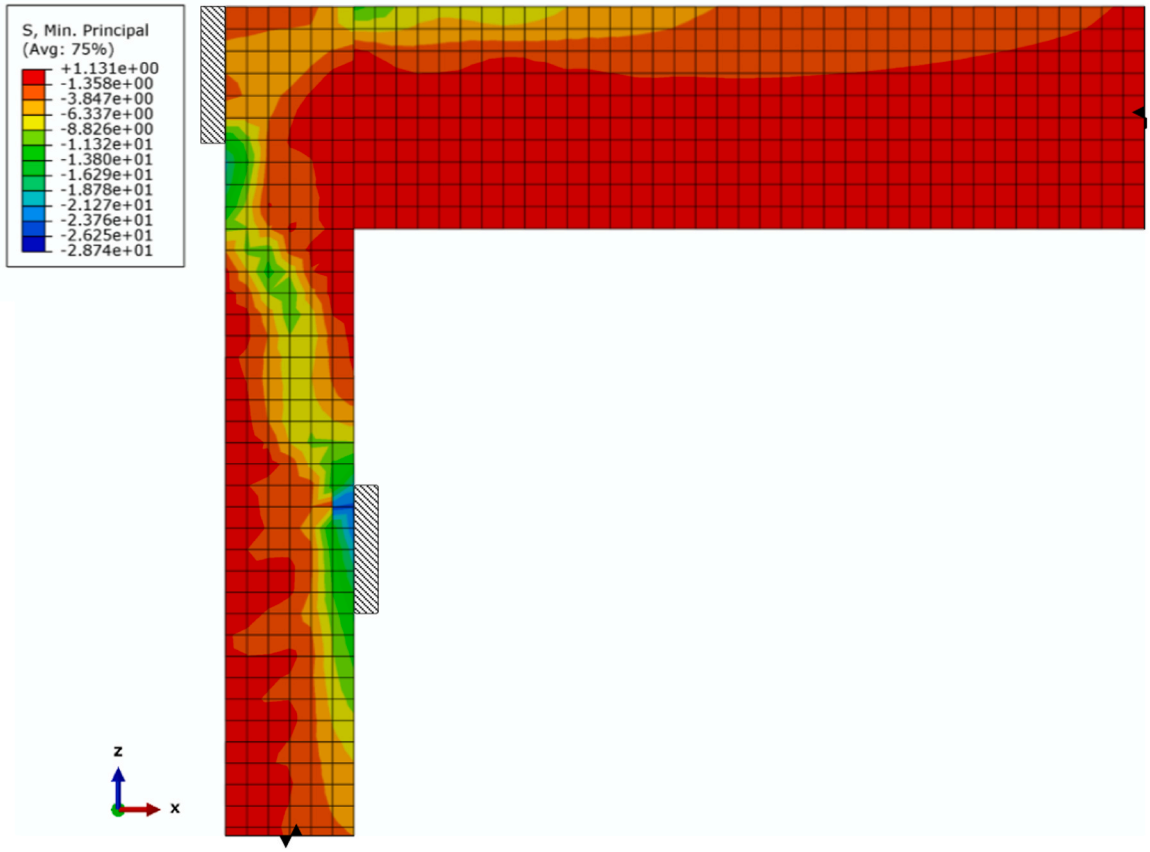

Fig. 8. Minimum principal stress field along short column and joint (displacement = 3.75 mm).

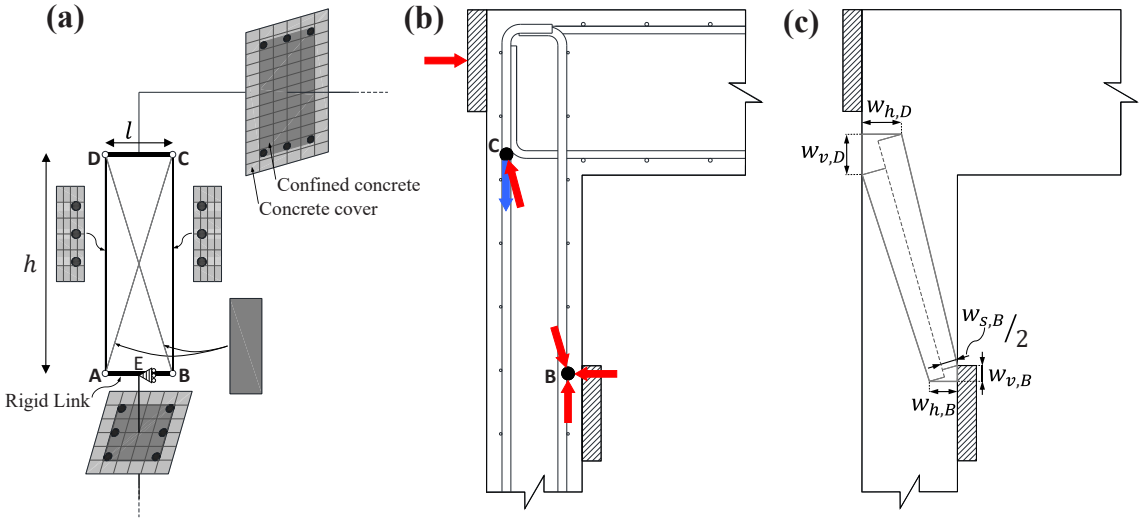

Fig. 9. New Short Column Macro Element (SCME) to model shear-flexure behaviour of short columns (a) SCME topology, (b) force distribution, and (c) strut and node formation.

4.2. New SCME

In this study, a new Short Column Macro Element (SCME) is proposed to model the behaviour of concrete short columns, as shown in Fig. 9a. The geometry of the SCME was defined using a strut-and-tie approach, as well as the experimental observations and numerical analyses of crack patterns and principal stress paths presented in Section 3.3.

In Fig. 9a, the bottom right node B is a CCC node created by the three compression forces shown in Fig. 9b: the reaction at the bearing face, the cross-sectional force at the back-face, and the force imposed by the strut. The width of the bearing face (see $w_{v,B}$ in Fig. 9c) was taken to be 25 mm based on the stress distribution at the interface between the column and the short-column boundary condition, as determined from the finite element analysis. Whilst the effect of the width of the bearing face on the strut angle and its size is minimal, the width of the bearing face was considered in the analysis to get a more precise location of the centroid of node B. For design, a more straightforward approach can be considered by assuming a negligible $w_{v,B}$, hence the node centroid would be at the bottom of the clear height of the short column (in this case at 300 mm down from the beam).

Likewise, the width of the back face $w_{h,B}$ (see Fig. 9c) was chosen to be equal to the neutral axis depth (i.e. 44 mm) at the yielding moment of the column, based on the centre of gravity of the compressive stress of the section. This is because the neutral axis depth represents the region in compression at that location. The width of the strut at node B ($w_{s,B}$ in Fig. 9c) was taken as the width normal to the centreline, according to Eq. (2):

$$w_{s,B} = w_{h,B}\sin\alpha + w_{v,B}\cos\alpha = 50 \text{ mm} \tag{2}$$

where $\alpha = \tan^{-1}h/l$ is the inclination angle of the strut, and h and l are the height and width of the SCME, respectively.

The width of the back face of the bottom left node A ($w_{h,A}$) of the SCME was equal to $w_{h,B}$. The width of the strut between points AC ($w_{s,A}$) was taken as the projection of $w_{h,A}$ onto the axis perpendicular to the strut:

$$w_{s,A} = w_{h,A}\sin\alpha \tag{3}$$

The top left node D (Fig. 9a) is a CCT node, created by the compression from the external load, the compression imposed by the strut, and the tension along the column's longitudinal reinforcement (Fig. 9b). Node D was located at the intersection of the centrelines of the column and beam's (bottom) longitudinal reinforcement of the tested building. The width of the horizontal ($w_{h,D}$) and vertical ($w_{v,D}$ in Fig. 9c) faces of node D was taken as twice the distance from the centreline of the reinforcement to the concrete face. Accordingly, $w_{h,D}$ = 62 mm and $w_{v,D}$ = 64 mm for the tested building. A constant strut width equal to the minimum width (i.e. $w_{s,C}$ = 50 mm) was considered in the analysis, as this captures the maximum resistance of the compressive strut. The depth of all SCME elements was equal to the column depth (150 mm in this case).

4.3. Material and element assignment for SCME

The diagonal struts AC and BD were modelled as truss elements made of plain concrete, using a *ConcreteCM* material in OpenSees. The negative effect of transverse tension on the concrete strength was considered using the approach included in Eurocode 2 [25], as defined by Eq. 4:

$$f_c^e = 0.6\left(1 - \frac{f_{cm}}{250}\right)f_{cm} \tag{4}$$

where f_c^e is the effective concrete compressive strength in the strut (in MPa). To account for the effect of confinement provided by the stirrups, the effective strength of the confined concrete (f_{cc}^e) was calculated using Mander et al.'s model [36] (Eq. 5):

$$f_{cc}^e = \varphi f_c^e \tag{5}$$

where φ is a confined strength ratio, found to be 1.10, which resulted in a value f_{cc}^e. = 21.0 MPa.

The post peak stress-strain behaviour of the strut was modified to consider its aspect ratio [37–39]. The Chang and Mander concrete model in OpenSees allows for the post peak branch to be adjusted by defining a shape factor r_c, which was originally proposed based on Tsai's uniaxial compressional model [40,41]. The factor r_c was calibrated based on the relationship proposed by Palmquist and Jansen [37], and its value was found to be r_c = 10 according to the calculations presented in Appendix A.

The two vertical elements AD and BC of the SCME (see Fig. 9a) were modelled as truss elements made of reinforced concrete, with widths $w_{h,A}$ and $w_{h,B}$, respectively. The concrete in these elements was modelled using the *ConcreteCM* material defined in OpenSees. The effect of the stirrup confinement was ignored for these edge vertical elements and therefore the concrete compressive and tensile strengths were taken as

$f_{cm} = 37.0$ MPa and $f_{ct} = 3.3$ MPa, respectively. Each element had three reinforcing bars according to the cross section of the columns. The bars were modelled using a *Steel02* material model with material properties as described in the experimental section of this study.

The horizontal elements AB and DC of the SCME were modelled as rigid links (see Fig. 9a) to allow the transference of moments and forces from the building to the SCME.

4.4. Analysis of tested building in OpenSees

4.4.1. Load and boundary conditions

The bottom of the columns was modelled as fully fixed. To simulate the short column, node E (located at the middle of the bottom rigid link of the SCME, Fig. 9a) was restrained against displacement in the X direction. A gravity nodal load of 13 kN (including self-weight) was applied at the top of each column under load control. A lateral pushover analysis was performed under displacement control via a nodal force at the top node of the left column, up to a maximum displacement of 6.0 mm.

4.4.2. Results and discussion

Fig. 10 compares the load vs displacement results obtained from OpenSees and Abaqus® models, as well as the backbone curve obtained from the tests on the building. The results indicate that the 2D frame modelled in OpenSees had an initial stiffness of 119 kN/mm, which is similar to that obtained from the finite element model on Abaqus®. The model reached a peak load of 142 kN at a displacement of 4.48 mm. Failure of the OpenSees model was due to the compressive failure of strut DC, which agrees well with the experimental observations. The results also show that, compared to Abaqus®, the load-displacement curve obtained from OpenSees matches better the experimental envelope. However, since the shear stirrups were not explicitly modelled in OpenSees, the horizontal shift in displacement recorded during the test and captured by Abaqus® at the onset of stirrup yielding could not be reproduced by the OpenSees model.

In the new SCME, the shear deformation is a function of the stiffness of the shear transfer mechanisms acting within the SCME. Fig. 11 shows the proportion of shear displacement δ_s (as % of the local short column deformation) within the short column for both OpenSees and Abaqus® models. In this figure, the shear displacements δ_s were decoupled from the flexural displacements using Massone and Wallace's model [42]. The

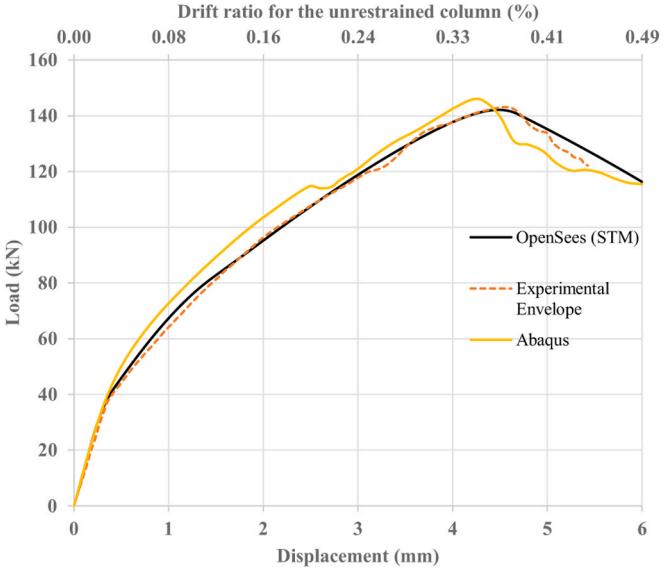

Fig. 10. Load vs displacement results from OpenSees, Abaqus® and experimental envelope results from tested building.

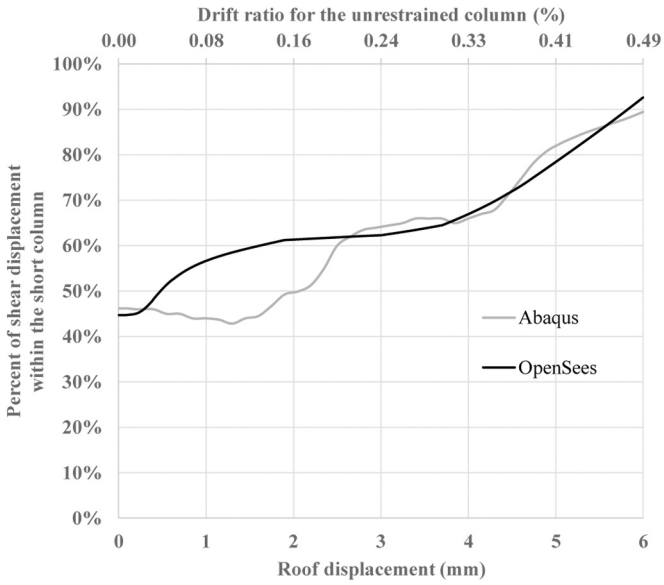

Fig. 11. Decomposition of shear-flexural displacement of short column (conventional concrete).

results in Fig. 11 show that both OpenSees and Abaqus® models calculate the initial δ_s to be 45% of the short column's total deformation. It is also shown that δ_s increases faster in the SCME (in OpenSees) as the global lateral displacement of the frame increases. This is because the SCME was specifically designed to deform in shear from the start of the analysis, whereas the strut and tie mechanism in Abaqus® can only form after the structure has undergone an initial amount of deformation. At higher displacements (>2.6 mm), however, both models calculate similar shear and flexural components of deformation. Moreover, the running time for the OpenSees simulation was only two minutes, whereas that of Abaqus® took an average of five hours to give results. This indicates that the new SCME proposed in this article can predict accurately the load-displacement behaviour of short columns throughout the entire load history (including the elastic behaviour, first cracking, peak capacity, and post-peak softening up to failure) with much less computational time. The results in Fig. 11 also indicate that the deformation capacity of the short columns was very limited, which results from the premature shear failure of the element.

4.4.3. Model validation

To investigate the accuracy of the new SCME at predicting results from short columns with different geometries and materials, the experimental results from short columns (Specimens 1 and 7) reported by Moretti and Tassios [18] were used. Specimen 1 had an aspect ratio of 1.0 ($l = 250$ mm, $h = 500$ mm), whereas Specimen 7 had an aspect ratio of 2.0 ($l = 250$ mm, $h = 1000$ mm). The two Specimens were tested in double curvature until failure. The unconfined concrete compressive strength of both Specimens was 36.0 MPa. Further details of the validation strategy are summarised in Appendix B. Figs. 12a-b compare the load vs displacement results obtained from the OpenSees model with the new SCME, as well as the backbone curve from Specimens 1 and 7 tested by Moretti and Tassios [18]. The results confirm that the proposed SCME captures well the behaviour of short columns, particularly for Specimen 1 that had a smaller aspect ratio. This is reasonable since the new SCME proposed in this study was explicitly developed for columns with short aspect ratio with predominantly shear-dominated behaviour.

The good agreement in results confirmed that the boundary conditions and general behaviour adopted in the new SCME replicate well the behaviour of short concrete columns of buildings. However, it is evident that the deformation capacity of the short columns was very limited. Accordingly, the following section uses the 2D frame model developed

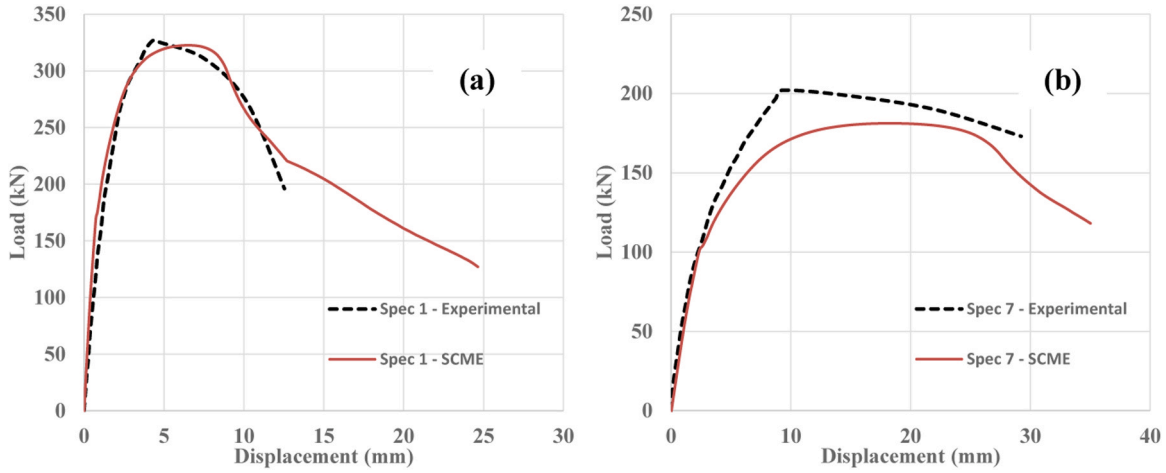

Fig. 12. Load vs displacement results from OpenSee and experimental envelope results from (a) Specimen 1 and (b) Specimen 7 tested by Moretti and Tassios [18].

in OpenSees and Abaqus® to examine numerically the feasibility of using highly deformable FRP CRuC to increase the deformability of short columns. It should be noted that whilst the results from the OpenSees model agree well with the test results and the numerical results from Abaqus®, further research should validate the applicability of the new SCME to other cases studies with different geometry to the short columns presented in this article.

5. Numerical investigation on highly deformable FRP CRuC short columns

Further numerical analyses on OpenSees and Abaqus® examined the behaviour of buildings with short columns made of FRP CRuC. A rubber content of 60% in the CRuC was assumed in the investigation. Previous studies by the authors [43] indicate that such level of aggregate replacement proved suitable to ensuring a high deformability in concrete, while also maintaining a good compressive strength for structural use. Aramid FRP (AFRP) confining jackets were chosen as these provide a good tensile strength at higher ultimate elongation compared to other confining materials [3]. In the analysis, the rupture strain of the AFRP jackets was taken as 65–70% of the ultimate sheet strain given by the manufacturer. This is justified as such values were found to match well actual sheet strains measured on AFRP CRuC cylinders tested in compression, as reported in a previous study by the authors [3]. The reduced ultimate strain of the jackets is lower than the uniaxial rupture strain of the sheet due to the fact that the jacket might have imperfections and stress concentrations, as demonstrated in previous research [23].

5.1. Numerical simulation of FRP CRuC short columns in Abaqus®

The Abaqus® model described in Section 3 was modified to carry out this analysis. The first modification included the separate modelling of: i) the short column using RuC instead of normal concrete, and ii) the addition of external AFRP jackets as confinement. The stress-strain behaviour of RuC was obtained from the constitutive model proposed by Bompa et al. [44], who used similar materials and percentage of rubber replacement as those use in the tested building. Table 1 summarises the material properties of the RuC adopted in the analysis. The dilation angle in the CDP model was increased to $\psi = 45^{\circ}$ to consider the high lateral dilation of RuC, as suggested in previous research [4,6].

The AFRP confinement was modelled as a shell-membrane, with a user-defined *Lamina* material model. Table 1 provides the material properties of the dry AFRP sheets as provided by the producer. A tie constraint was used to connect the AFRP jacket to the concrete surface, assuming perfect bond between the two surfaces.

Table 1
Material properties of RuC proposed by Bompa et al.'s model and AFRP properties.

Conventional concrete	f_{cm}	-	-	-	-	-
Benchmark concrete [44]	63	-	-	-	-	-
RuC	ρ_{vr} (%)	λ	E_{rc}	f_{rc}	ε_{rc}	$f_{rc,t}$
60% rubber replacement	60	2.9	9.2	6.7	0.105	0.92
AFRP CRuC	f_{cr}	ε_{cr}	f_{crc}	ε_{crc}	f^{e}_{crc}	ε^{e}_{crc}
1L (1 Layer of AFRP)	8	0.14	28	3.00	26	2.77
2L (2 Layers of AFRP)	10	0.17	47	4.34	44	4.00
3L (3 Layers of AFRP)	12	0.19	66	5.42	61	5.00
Aramid FRP	t (mm)	E_f	f_u	ε_{fu}	-	-
S&P A120/290	0.2	116	2400	2.5	-	-

Strength f in (MPa), Young's modulus E in GPa, and strain in %

In Table 1, ρ_{vr} is the percentage of rubber replacement by volume; λ is a factor for the type of rubber used (λ=2.9 for a coarse and fine rubber); whereas E_{rc}, f_{rc}, ε_{rc}, and $f_{rc,t}$ are the Young's modulus, peak compressive strength, strain at peak compressive strength, and peak tensile strength for unconfined rubberised concrete, respectively. The latter variables and corresponding values were adopted from Bompa et al.'s model [44]. For the AFRP CRuC part of the table, f_{cr} and ε_{cr} are the critical stress and strain, respectively [45]; f_{crc} and ε_{crc} are the ultimate compressive strength and strain of AFRP CRuC, respectively; f^{e}_{crc}, and ε^{e}_{crc} are the effective ultimate compressive strength and strain of AFRP CRuC, respectively, which account for the inclination of the strut in the new SCME model. Note that the critical stress f_{cr} and corresponding strain ε_{cr} represent the start of unstable crack propagation and concrete expansion, which in turn activate the confining jacket and change the gradient of the stress-strain constitutive curve of AFRP CRuC (see Figure C1 in Appendix C). Full details of the AFRP CRuC constitutive model can be found in Raffoul et al. [45].

In Table 1, the dry AFRP properties t, E_f, f_u, and ε_{fu}, are the dry sheet thickness, Young's modulus, ultimate rupture strength, and strain at rupture, respectively, as given by the AFRP producer.

Based on the above material properties, three frames were modelled assuming AFRP jackets with 1, 2 or 3 layers around the short columns. Such three frame models are identified in Table 1 and in subsequent sections/tables as 1L, 2L, and 3L, respectively. A lateral displacement was imposed at the top of the column until "failure" of the frame model occurred.

5.1.1. Results and analysis of numerical simulations

Fig. 13 compares the load vs displacement curves obtained from Abaqus® for models 1L, 2L, and 3L. The figure also includes the envelope load-displacement curve of the building tested in this study (made

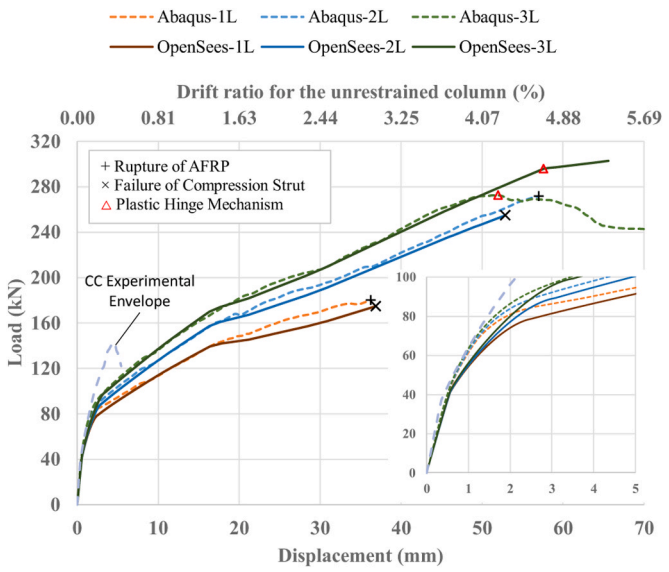

Fig. 13. Load vs displacement of frame models with AFRP CRuC short columns, results from Abaqus® and OpenSees with new SCME.

of CC), as well as OpenSees results to be discussed later in Section 5.2. The behaviour of the three frame models shown in Fig. 13 can be described by four distinctive phases:

1) *Elastic Phase I*, which is not affected by the level of confinement as the AFRP is not yet activated at this stage. The initial stiffness of all frames was around 83 kN/mm.
2) *Transition Phase II*, where the loss in stiffness is due to the development of cracking at the short column/beam interface. At the onset of this phase, the compressive stresses developed within the short column cause its lateral expansion, which in turn activates the AFRP jackets. This phase ends when the RuC reaches its peak strength, which occurs at higher strain values for increasing values of confinement stiffness. This phase ends at a lateral load of 83 kN, 94 kN, and 102 kN for frames 1L, 2L and 3L, respectively.
3) *Linear hardening Phase III*, which stiffness is determined by the level of confinement along with the strength from all other structural elements. The stiffness of this branch was 4.3, 5.4, and 6 kN/mm for frames 1L, 2L and 3L, respectively.
4) A further reduction in stiffness (*Phase IV*) is observed due to yielding of the longitudinal reinforcement at the bottom of unrestrained column C1B (hinge formation), which occurs after a lateral displacement of approximately 19 mm for all three confinement levels.

Phase IV ends with the failure of the frame model. Models 1L and 2L failed when the AFRP reached its rupture strain of 1.75%, which occurred at lateral displacements of 36 mm (2.9% drift ratio) and 57 mm (4.6% drift ratio), respectively. Conversely, frame 3L failed following the formation of a plastic hinge mechanism when the longitudinal reinforcement in column C1A yielded at the short column restraint level, which occurred at a frame displacement of 52 mm and a lateral load of 272 kN. At this stage, the strain in the AFRP was 1.3%.

It should be noted that the load-displacement behaviour described above is in line with that observed by Wang et al. [16] (see Figure C2 in Appendix C). Indeed, Wang et al. proved that the load-displacement behaviour of rectangular prisms confined with FRP CRuC tested in shear also presented four characteristic phases, as discussed by El Khouri [29]. The results from Abaqus® confirm that whilst the behaviour of the frame was dominated by the short column effects, the replacement of conventional concrete with AFRP CRuC improved the frame's performance by increasing the deformability of the short column.

Fig. 14 shows the strain profile vs displacement obtained from Abaqus® for the three frame models 1L, 2L, and 3L. The results were obtained at the centre of the AFRP sheet along the faces of the column both parallel (X direction) and perpendicular (Y direction) to the loading direction. It is shown that, as expected, the FRP strains in the loading direction were higher than the strains in the transverse direction as the fibres resisted the development of diagonal cracking. Moreover, the FRP strains decreased as the amount of FRP layers increased, which in turn led to a more uniform distribution of strains around the column perimeter. For example, at a drift ratio of 2.44% for the unrestrained column (30 mm frame displacement), the strain in the AFRP along the loading direction reached 1.4% for model 1L, while strain levels of 1.03%, and 0.82% were recorded for models 2L and 3L, respectively.

5.2. Modelling FRP CRuC short columns using the proposed SCME in OpenSees

The proposed SCME was modified to model the AFRP CRuC short column in OpenSees. Accordingly, the constitutive model developed by Raffoul et al. [45] was used here to i) define the uniaxial compressive behaviour of AFRP CRuC, which implicitly considers the effect of different confinement stiffnesses (i.e. different jacket thickness and type of FRP), and to ii) determine the relevant parameters of the *Concrete02* material model in OpenSees.

Since the fibres of the AFRP jacket around the short column were assumed as horizontal (i.e. perpendicular to the column axis), and because the strut is inclined at an angle of $\alpha = \tan^{-1} h/l$ as per Eq. 2, the effectiveness of the confinement to the compressive strut had to be reduced. To account for the reduced effectiveness of the confinement due to the relative inclination between the confining FRP fibres and the strut, the ultimate strength f^{e}_{crc} of the AFRP CRuC was reduced using Eq. 6.

$$f^{e}_{crc} = (f_{crc} - f_{cr})\sin^2\alpha + f_{cr} \tag{6}$$

where f_{crc} and f_{cr} are defined as the compressive strength and critical stress of the AFRP CRuC, respectively [45] (see Figure C1 in Appendix C).

Consequently, the ultimate strain, ε_{crc}, was also reduced at a ratio that maintains the second linear stiffness of the AFRP CRuC stress-strain relationship (Table 1). The material properties of the vertical elements of the SCME (AD and BC in Fig. 9a) were not reduced. The same

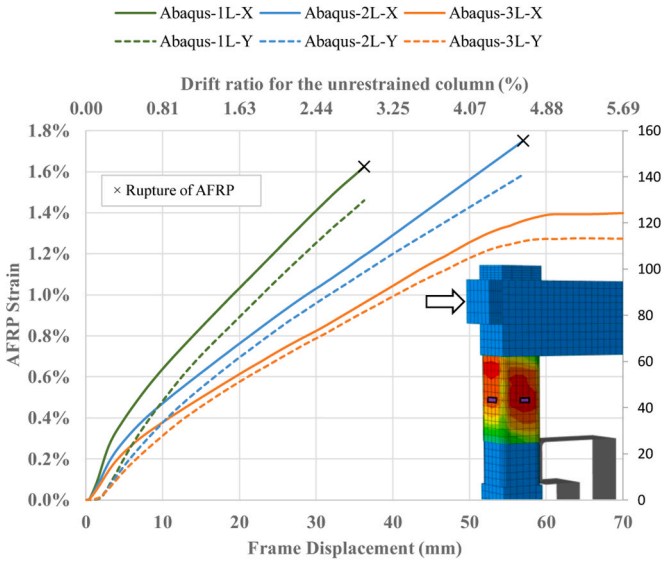

Fig. 14. Numerical lateral strains at centre of AFRP jacket in directions parallel (X) and perpendicular (Y) to loading direction, results obtained from Abaqus®.

boundary conditions and dimensions of the SCME with conventional concrete were also used for the AFRP CRuC SCME.

5.2.1. Results and analysis of the AFRP CRuC SCME simulations

Fig. 13 compares the load vs displacement curves of frames 1L, 2L and 3L with the AFRP CRuC SCME obtained from OpenSees. The results show that the *transition Phase II* was slightly softer in OpenSees than in Abaqus®. However, up to the peak strength of the RuC, the OpenSees results agreed well with those from the more advanced analysis in Abaqus®. The elastic stiffness for all three frames was around 77 kN/mm, whereas the stiffness of the *linear hardening Phase III* was 4.4, 5.2, and 5.6 kN/mm for frames 1L, 2L and 3L, respectively. At a lateral frame displacement of 16.8 mm, the steel at the bottom of the unrestrained column yielded for all three frame models, thus indicating the start of *Phase IV*. Frame models 1L and 2L failed when the strut reached its maximum strength, corresponding to the theoretical rupture of the AFRP jacket at a lateral displacement of 37 mm (3.0% drift ratio) and 52 mm (4.2% drift ratio), respectively. These results indicate that the use of FRP CRuC in the short column was very effective at increasing the deformation capacity of the building. Indeed, whilst the tested building failed at a small displacement of 5.4 mm (0.43% drift ratio), the use of FRP CRuC short columns with minimal confinement (one layer of AFRP only) increased the building's displacement by almost seven times to 37 mm (3.0% drift ratio).

On the other hand, frame model 3L failed due to the formation of a plastic hinge mechanism (which is consistent with the Abaqus® results) at a displacement of 57 mm and a lateral load of 295 kN. The results in Fig. 13 also confirm that the SCME in OpenSees simulated accurately the four-phase load-displacement behaviour observed in shear tests on rectangular prisms confined with FRP CRuC [16]. This provides further confidence on the suitability of the new SCME at predicting the behaviour of short columns made of FRP CRuC. The ductility of the frames was assessed based on the bilinear idealisation of the force-displacement curve according to FEMA 356 [46]. The displacement ductility values obtained from OpenSees were 18.9, 22.9, and 22.3 for the frame models 1L, 2L and 3L, respectively, which are somehow similar to those obtained from the analyses in Abaqus®.

Whilst the AFRP jacket was not explicitly modelled in the SCME in OpenSees, it was possible to estimate the lateral strain of the jacket using the uniaxial compressive strain levels of the strut obtained from the OpenSees results, and the equation of the adopted constitutive model for AFRP CRuC [45,47]. Fig. 15 compares the AFRP strains obtained from the SCME in OpenSees and those obtained from Abaqus®. The results in the figure show that the two curves are very similar up to the theoretical rupture strain of the AFRP jacket. This confirms that the new SCME is very effective at capturing the confining effect of the AFRP jacket.

5.3. Comparison between frame models with CC and CRuC short columns

The results in previous sections proved that short columns made of FRP CRuC can develop higher deformability than CC counterparts. This in turn led to a better utilisation of materials in the frame models since damage distributed more unfirmly among other structural elements, rather than being concentrated only in the short columns. For instance, while using CC in the short column limited the deformability of the frame model and prevented yielding of the longitudinal reinforcement, yielding occurred in the longitudinal bars of column C1B for all three models 1L, 2L and 3L. The higher ductility of the three AFRP CRuC frame models can be attributed to the unique mechanical properties of FRP CRuC, which enabled large shear deformations in the short column [16].

Fig. 16 shows the shear-flexure displacement decomposition of the AFRP CRuC short column for model 3L. Both results from Abaqus® and OpenSees with the new SCME are included. It is shown that the shear deformation of the short column accounts for 80–90% of the total frame deformations after a global displacement > 5 mm (0.4% drift ratio), i.e. once the frame model enters the *transition Phase II* that activates the AFRP jackets.

The numerical investigation presented in this article confirms that FRP CRuC can be used in high shear demand regions of buildings, which in turn can lead to a more ductile behaviour when compared to conventional concrete (CC) counterparts. However, since the proposed model SCME was calibrated with CC short columns, further research should verify experimentally the applicability of the new SCME to RuC and FRP CRuC. Moreover, research on FRP CRuC elements subjected to shear is scarce in the literature, and therefore future research should validate the accuracy of the model using other experimental datasets that include different types of FRP materials (such as Glass or Basalt FRP). A thorough parametric analysis is also necessary to assess the validity of the proposed numerical models in relation to the assumed modelling parameters.

It should be finally mentioned that the authors have also carried out shake table tests on buildings with short columns made of conventional

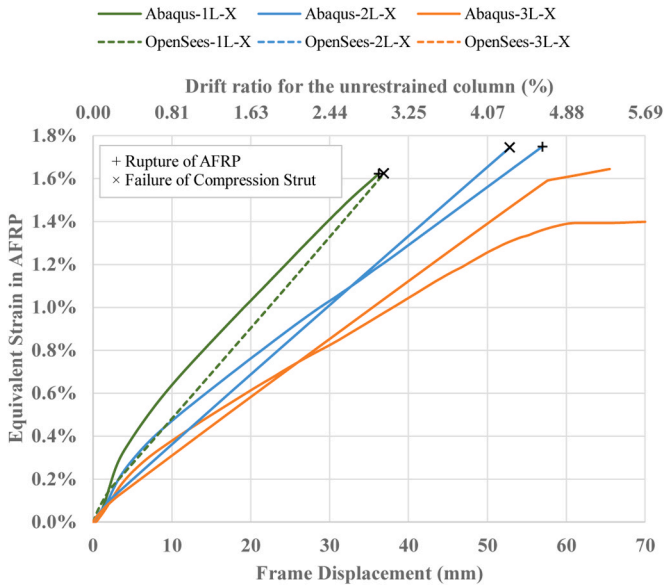

Fig. 15. Lateral strain in AFRP jackets for frame models with AFRP CRuC short columns, results from Abaqus® and OpenSees with new SCME.

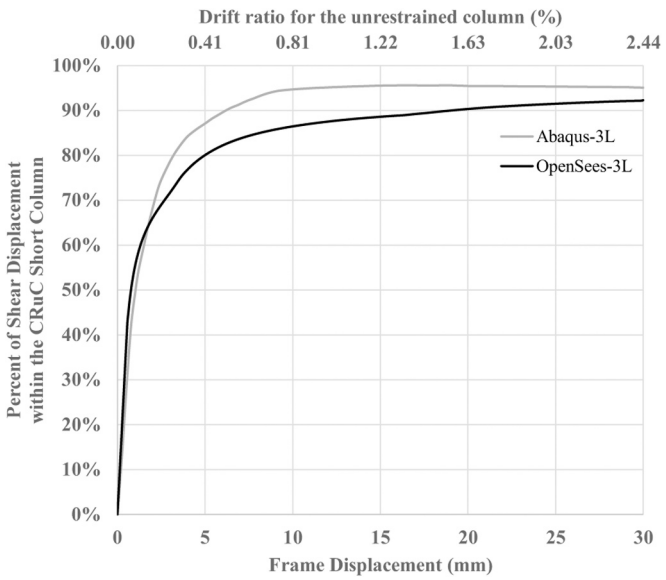

Fig. 16. Decomposition of the shear-flexural displacement of short column (CRuC-3L up to 30 mm lateral displacement of the frame).

concrete or FRP CruC [48]. The geometry, detailing, material properties and number of AFRP jackets examined in these tests were similar to those of frame model 3 L, discussed in Section 5 of this study. The results from these shake table tests confirmed that the use of highly deformable AFRP CRuC increased the drift capacity of the short columns by a factor of 3 over a counterpart frame with conventional short concrete columns. These experimental results are thus fully aligned with the numerical findings discussed in Section 5 of this study. Due to space limitations, the results of these shake table tests will be reported in a forthcoming article.

6. Summary and conclusions

This article proposed a new and practical Short Column Macro Element (SCME) that predicts accurately the behaviour of short concrete columns. A 1/3-scale one-storey building with short columns made of conventional concrete was subjected to lateral loading tests until failure. The experimental results from the building are then used to calibrate a numerical model in Abaqus®. The experimental crack patterns and stress distribution from Abaqus® were used to determine the load path within the short column. Based on this information, a new strut-and-tie SCME was proposed and implemented in OpenSees. Subsequently, the frame models calibrated in OpenSees and Abaqus® were modified to examine numerically the effectiveness of highly deformable FRP CRuC at increasing the deformability of short columns with different levels of FRP confinement (1, 2 or 3 layers). Based on the results of this study, the following conclusions can be drawn:

- Failure of the tested building made of conventional concrete was dominated by the brittle shear failure of the short columns. Failure occurred at a small displacement of only 5.4 mm (0.43% drift ratio) for the unrestrained column. The building did not develop any ductility as the longitudinal reinforcement of all elements remained withing the elastic range.
- The 2D model of the building in Abaqus® was effective at providing details of the evolution of the main load transfer mechanism within the short columns. The analytical stress distribution obtained from the numerical analyses agreed very well with the experimental cracking pattern. It also provided insight into the evolution of the main load transfer mechanism within the short columns.
- The new SCME captured accurately the behaviour of the short columns of the tested building modelled in OpenSees. For the tested building, the OpenSees results predicted accurately the load-displacement behaviour of short columns throughout the entire load history (elastic behaviour, first cracking, peak capacity, and post-peak softening up to failure). Compared to Abaqus®, the load-displacement curve obtained from the OpenSees model matched better the experimental envelope of the building. Moreover, the adoption of the SCME in OpenSees significantly reduced computational time to minutes rather than hours for the analysed building. The new SCME also predicted well the results from short columns with different geometries and materials reported in the literature.
- The proposed SCME was modified to account for the use of highly deformable FRP CRuC in short columns. The numerical results show that FRP CRuC short columns have a four-phase load-displacement behaviour consistent with previous shear tests on FRP CRuC prisms. This confirmed the suitability of the new SCME at predicting the behaviour of short columns made of FRP CRuC.
- The use of highly deformable FRP CRuC in short columns significantly improved the performance of the frame models analysed in OpenSees. Whilst the tested building failed at a small displacement of 5.4 mm (0.43% drift ratio), the numerical analysis showed that use of FRP CRuC short columns with minimal confinement (one layer of AFRP only) increased the building's displacement by almost seven times to 37 mm (3.0% drift ratio). This also enabled more redistribution of forces to other structural members.

CRediT authorship contribution statement

Imad El Khouri: Conceptualization, Data curation, Formal analysis, Investigation, Methodology, Software, Validation, Visualization, Writing – original draft. **Reyes Garcia:** Conceptualization, Funding acquisition, Investigation, Methodology, Supervision, Validation, Visualization, Writing – original draft, Writing – review & editing. **Petru Mihai:** Formal analysis, Investigation, Methodology, Software, Supervision. **Mihai Budescu:** Funding acquisition, Investigation, Project administration, Resources, Supervision. **Nicolae Taranu:** Conceptualization, Funding acquisition, Investigation, Methodology, Project administration, Resources. **Ionut Ovidiu Toma:** Funding acquisition, Investigation, Methodology, Project administration, Supervision. **Maurizio Guadagnini:** Conceptualization, Formal analysis, Investigation, Project administration, Supervision, Writing – original draft. **David Escolano-Margarit:** Formal analysis, Investigation, Software, Validation. **Ioana Sorina Entuc:** Formal analysis, Validation. **Gabriel Oprisan:** Formal analysis, Validation. **Iman Hajirasouliha:** Conceptualization, Formal analysis, Funding acquisition, Methodology, Project administration, Supervision, Validation, Writing – review & editing. **Kypros Pilakoutas:** Conceptualization, Funding acquisition, Investigation, Methodology, Project administration, Supervision, Writing – review & editing.

Declaration of Competing Interest

The authors declare that they have no known competing financial interests or personal relationships that could have appeared to influence the work reported in this paper.

Data availability

No data was used for the research described in the article.

Acknowledgments

The research leading to these results has received funding from the European Union Seventh Framework Programme [FP7/2007–2013] under grant agreement n° 603722. The authors would like to thank the technical staff at the Civil Engineering Laboratory at the Technical University Gheorghe Asachi (Iasi, Romania) for their support to conduct the tests reported in this article.

Appendix A. Calibration of the shape factor r_c in Chang and Mander's concrete stress-strain model

Eq. A1, developed by Tsai and implemented in Chang and Mander's model, gives the stress-strain relation for unconfined concrete:

$$y = \frac{nx}{1 + \left(n - \frac{r_c}{r_c - 1}\right)x + \frac{x^{r_c}}{r-1}} \tag{A1}$$

$$x = \frac{\varepsilon_c}{\varepsilon_{cm}} \tag{A2}$$

$$y = \frac{\sigma_c}{f_{cm}} \tag{A3}$$

where ε_c and σ_c are the compressive strain and stress, respectively; ε_{cm} is the compressive strain at peak stress; n and r_c are parameters that control the shape of the stress-strain curve and are defined by Chang and Mander as follows:

$$n = \frac{7.2}{f_{cm}^{3/8}} \tag{A4}$$

$$r_c = \frac{f_{cm}}{5.2} - 1.9 \tag{A5}$$

Eqs. A1-A5 provide the full stress-strain curve of a concrete cylinder as a function of the peak strength and strain.

Palmquist and Jansen developed Eqs. A6 - A8 to calculate the post-peak strain taking into account the aspect ratio of the element under compression:

$$\varepsilon = \left(\varepsilon_{cm} + \frac{\sigma_c - f_{cm}}{E_c}\right)\frac{H_B}{H} + \frac{1}{V}\left(\frac{f_{cm}}{\sigma_c} - N\right)^M \frac{H_D}{H} \tag{A6}$$

$$H_B = H - H_D \tag{A7}$$

$$H_D = W\left(2 - \frac{\sigma_c}{f_{cm}}\right) \tag{A8}$$

where H is the height of the specimen; H_D is the height of the damage zone in the specimen; and $H_B$is the height of the bulk zone beyond the damage zone (see Figure A1). Likewise, M, N and V in Eq. A6 are empirical constants calibrated for each type of concrete based on the full stress-strain curve.

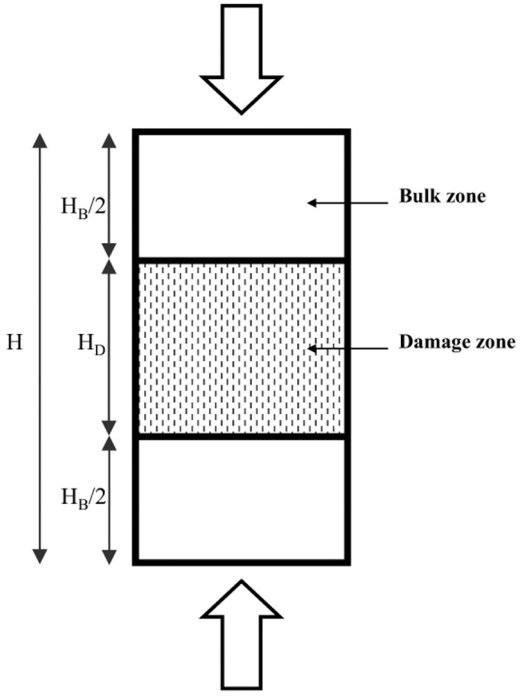

Fig. A1. Definition of the compression damage zone according to Palmquist and Jansen. [37].

Palmquist and Jansen's post-peak strain model was calibrated to fit the stress-strain curve of Chang and Mander for a standard 100 × 200 mm cylinder tested in compression (see Figure A2, for an initial shape factor $r_c = 5.2$). The empirical constants were found to be equal to 0.145, 0.992, and 225 for M, N and V, respectively.

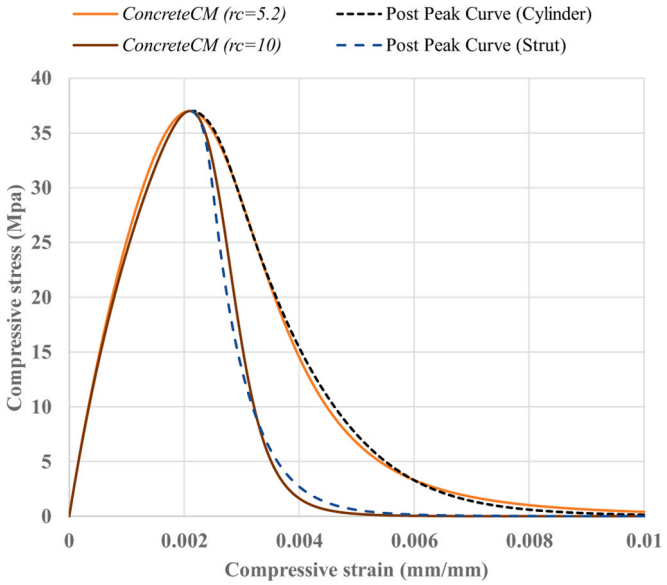

Fig. A2. Calibration of the Shape Factor r_c in Chang and Mander's compressive stress-strain model to account for the slenderness ratio of a concrete strut [40].

The post-peak behaviour was then modified according to the aspect ratio of the strut, which was calculated based on the equivalent diameter of the rectangular area (equal to 97 mm) and an element length of 358 mm. The shape factor r_c was then calibrated to fit the new post-peak behaviour for the strut (see Figure A2), which resulted in a shape factor $r_c = 10$.

Appendix B. Validation of new SCME

The validation was done using Specimens 1 and 7 tested by Moretti and Tassios [18]. The experimental programme involved columns of same cross-section but varying length. Specimen 1 had an aspect ratio equal to 1 (width of 250 mm, length of 500 mm) and somehow similar to the short column in the scaled-down building presented in this article. Specimen 7 had an aspect ratio equal to 2 (with of 250 mm, length of 1000 mm). The columns were reinforced with eight 14 mm longitudinal bars (Figure B1a) which had yield and ultimate strengths of $f_{ly} = 480$ MPa and $f_{lu} = 740$ MPa, respectively. The shear reinforcement consisted of one tie and two cross-ties at a spacing of 50 mm, having a yield strength of $f_{sy} = 300$ MPa. The columns were tested in a double curvature as shown in Figure B1b.

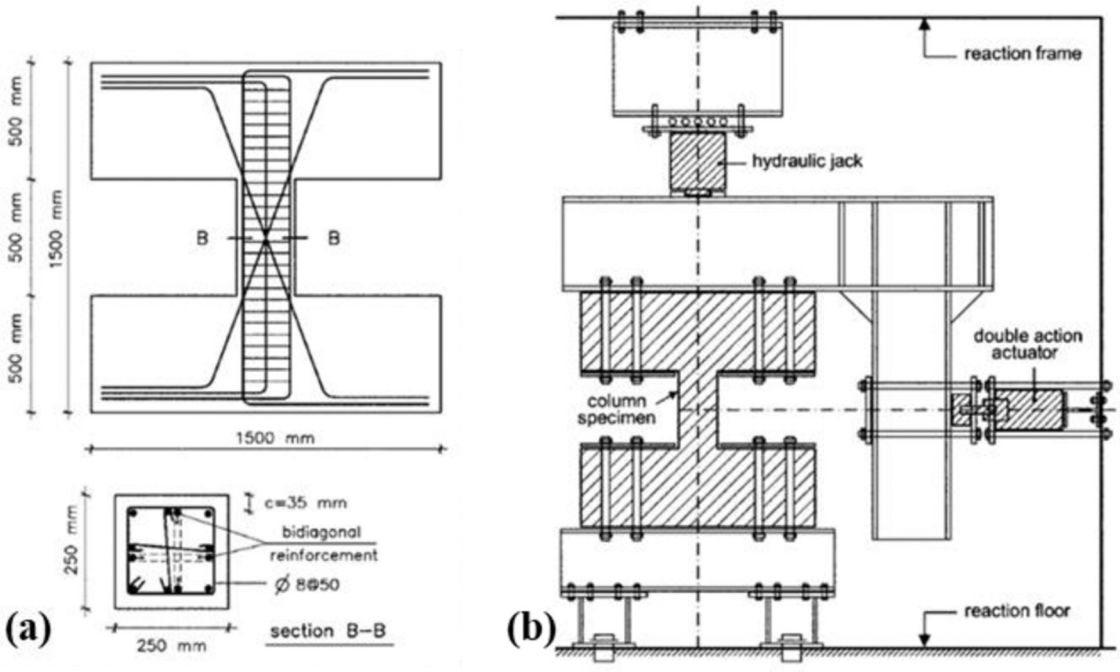

Fig. B1. (a) Specimen cross-section and reinforcement, and (b) test setup [18].

Using the same topology described in Section 4.2 (as shown in Figure B2), the geometry of the SCME for the validation on OpenSees was obtained as described below.

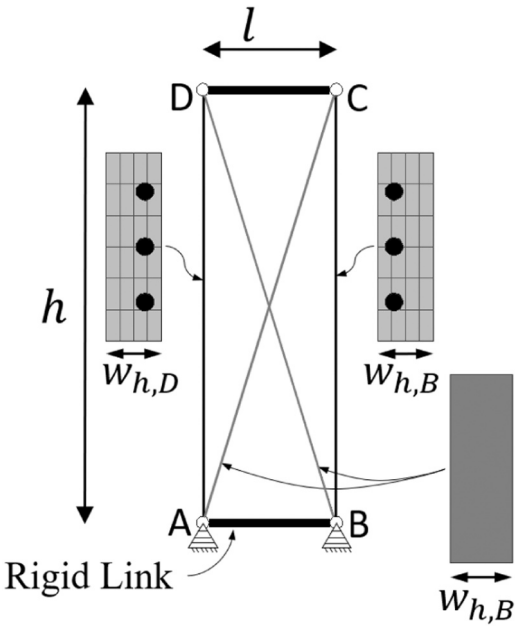

Fig. B2. SCME topology and boundary conditions used to model Specimens 1 and 7 in OpenSees.

The width of the node face $w_{h,B}$ at node B was chosen to be equal to the neutral axis depth (calculated to be 67 mm) at the yielding moment of the column, based on the centre of gravity of the compressive stress of the section. The neutral axis was calculated using a moment-curvature analysis. Due to symmetry of the cross-section, the following values were taken $w_{h,B} = w_{h,A} = w_{h,D} = w_{h,C}$. In the case of double curvature bending tests, there are no vertical nodes or strut supports, which simplifies the dimensioning of the struts, as mentioned in the main text. The width of the diagonal struts is simply taken as the width of the nodes (67 mm). The depth of all SCME elements was equal to the column depth of 250 mm.

The diagonal struts AC and BD were modelled as truss elements made of plain concrete, using *ConcreteCM* material in OpenSees. The effective concrete compressive strength in the strut was calculated to be 18.5 and 19.3 MPa for Specimens 1 and 7, respectively. Based on Mander et al.'s confinement model, the confined strength ratio φ was 1.4. The effective strength of the confined strut was 26 and 27 MPa for Specimens 1 and 7, respectively. The shape factor r_c was calibrated to be 12.

The two vertical elements AD and BC of the SCME were modelled as truss elements made of reinforced concrete with material definitions as given by Moretti and Tassios [18].

The model boundary conditions were set to force a double curvature, and a monotonic increasing displacement was applied to reach failure. The results from the validation are discussed in Section 4.4.3 of the article.

Appendix C. Axial, lateral, and shear stress-strain behaviour of FRP CRuC

Figure C1 shows the stress-strain model adopted for the analysis of FRP CRuC concrete. The constitutive model was extensively calibrated with results from cylinders confined with Carbon and Aramid FRP CRuC under uniaxial compression [3,23,45].

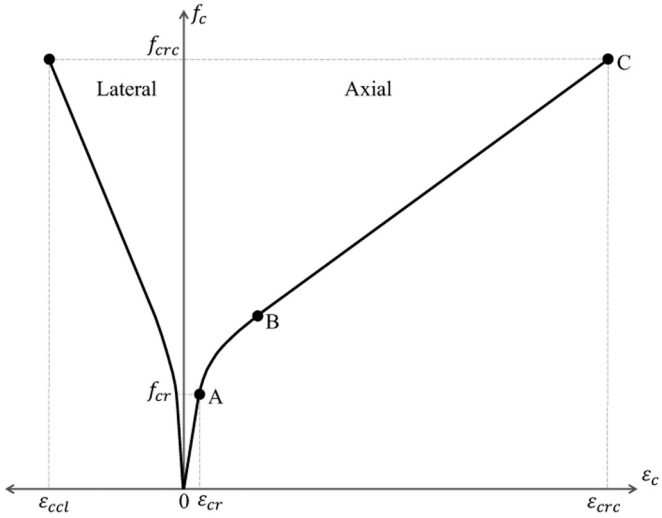

Fig. C1. Schematic axial and lateral stress-strain behavior of CRuC.

Figure C2 shows the shear stress-strain model adopted from Wang et al. [16]. The three phases of the shear stress-strain documented by

Wang match the results obtained in the short column lateral behaviour. The additional fourth phase shown in the figure describes the case of no-rupture of FRP and yielding of the structure that would exhibit a ductile yielding.

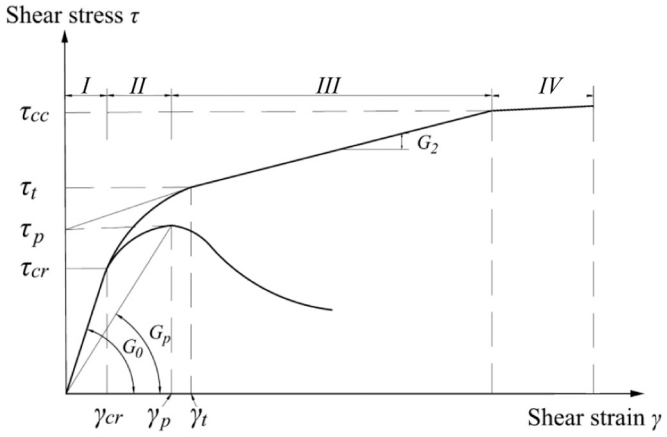

Fig. C2. Schematic shear stress-strain behavior of CRuC adopted from Wang et al. [16].

References

[1] ACI Committee 318. Building Code Requirements for Structural Concrete (ACI 318–14) and Commentary, Farmington Hills, MI, 2014, 519 pp.
[2] EN 1998–1. Eurocode 8: Design of structures for earthquake resistance - Part 1: General rules, seismic actions and rules for buildings, Comité Européen de Normalisation (CEN), Brussels Belgium, 2004.
[3] Raffoul S, Garcia R, Escolano-Margarit D, et al. Behaviour of unconfined and FRP-confined rubberised concrete in axial compression. Constr Build Mater 2017;V. 147:388–97.
[4] Youssf O, Elgawady MA, Mills JE, et al. An experimental investigation of crumb rubber concrete confined by fibre reinforced polymer tubes. Constr Build Mater 2014;V. 53:522–32.
[5] Lam L, Teng JG. Design-oriented stress–strain model for FRP-confined concrete. Constr Build Mater 2003;17:471–89.
[6] Duarte APC, Silva BA, Silvestre N, De Brito J, Júlio E, Castro JM. Tests and design of short steel tubes filled with rubberised concrete. Eng Struct 2016;112:274–86.
[7] Raffoul S, Escolano-Margarit D, Garcia R, Guadagnini M, Pilakoutas K. A new cyclic model for FRP-confined rubberized concrete. Struct Concr 2023;24(1):1627–41.
[8] Cao Y, Liu Y, Li X, Wu Y. Axial stress strain behavior of FRP-confined rectangular rubber concrete columns with different aspect ratio. Eng Struct 2023;297:116987.
[9] Skyrianou I, Valiakou EI, Koutas LN, Papakonstantinou CG. Behaviour of carbon or glass FRP-confined rubberised concrete under monotonic compression. Constr Build Mater 2023;406:133287.
[10] Elghazouli A, Bompa D, Xu B, et al. Performance of rubberised reinforced concrete members under cyclic loading. No. November 2017 Eng Struct 2018;V. 166: 526–45.
[11] Ismail MK, and, Hassan AAA. Performance of full-scale self-consolidating rubberized concrete beams in flexure. ACI Mater J 2016;V. 113(No. 2):207–18.
[12] Son KS, Hajirasouliha I, and, Pilakoutas K. Strength and deformability of waste tyre rubber-filled reinforced concrete columns. Constr Build Mater 2011;V. 25(No. 1): 218–26.
[13] AbdelAleem BH, and, Hassan AAA. Influence of rubber content on enhancing the structural behaviour of beam–column joints. Mag Concr Res 2018;V. 70(No. 19): 984–96.
[14] Bompa DV, and, Elghazouli AY. Behaviour of confined rubberised concrete members under combined loading conditions. Mag Concr Res 2021:1–19.
[15] Xu B, Bompa DV, Elghazouli AY, et al. Behaviour of rubberised concrete members in asymmetric shear tests. Constr Build Mater 2018;V. 159:361–75.
[16] Wang Z, Chen L, Guadagnini M, et al. Shear Behavior Model for FRP-Confined and unconfined rubberized concrete. J Compos Constr 2019;V. 23(No. 5):04019039.
[17] Yamada, M., and Furui, S. Research on the shear resistances of reinforced concrete members subjected to axial load, 1966.
[18] Moretti ML, Tassios TP. Behavior and ductility of reinforced concrete short columns using global truss model. Acids Struct J 2006;V. 103(No. 3):319–27.
[19] Yamada, M., and Furui, S. Shear resistance and explosive cleavage failure of reinforced concrete members subjected to axial load. Final report, 8th international congress IABSE, 1968. pp. 1091–1102.
[20] Wakabayashi, M., and Minami, K. An experimental study on hysteretic characteristics of reinforced concrete columns failing in shear. Proceedings of the 18th national symposium on bridge and structural engineering, 1972. pp. 97–112.
[21] Zhou W, Hong HP. Modeling error of strength of short reinforced concrete columns. Acids Struct J 2000;V. 97(No. 3):427–35.
[22] Mazzoni, S., McKenne, F., Scott, M.H., et al. Open System for Earthquake Engineering Simulation User Manual, Version 2.0, 2009.
[23] Raffoul S, Margarit DE, Garcia R, Guadagnini M, Pilakoutas K. A new cyclic model for FRP-confined rubberized concrete. Struct Concr 2023;V. 24(No. 1):1627–41.
[24] Anaggenisi: Innovative Reuse of All Tyre Components in Concrete, A Europear Commission Seventh Framework Programme, Grant agreement ID: 603722 https://cordis.europa.eu/project/id/603722.
[25] EN 1992–1-1. Eurocode 2: Design of concrete structures - Part 1–1: General rules and rules for buildings, Brussels Belgium, Comité Européen de Normalisation (CEN), 2004, 225 pp.
[26] EN 12390–3. Testing hardened concrete Part 3: Compressive strength of test specimens, Comité Européen de Normalisation (CEN), 2019.
[27] EN 10080. Steel for the reinforcement of concrete: Weldable reinforcing steel, General, Comité Européen de Normalisation (CEN), 2009.
[28] Dassault Systèmes SIMULIA. ABAQUS Software and Documentation, Ver 6.14, 2017.
[29] El Khouri, I. Highly deformable confined rubberised concrete elements for seismic applications, PhD thesis, Dept. of Civil and Structural Engineering, The University of Sheffield, 2021.
[30] Krätzig WB, and, Pölling R. An elasto-plastic damage model for reinforced concrete with minimum number of material parameters. Comput Struct 2004;V. 82(Nos. 15–16):1201–15.
[31] Hordijk DA. Tensile and tensile fatigue behaviour of concrete; experiments, modelling and analyses. Heron 1992;37(1):1–79.
[32] Alfarah B, López-Almansa F, and, Oller S. New methodology for calculating damage variables evolution in plastic damage model for RC structures. Eng Struct 2017;V. 132:70–86.
[33] Bažant ZP, and, Becq-Giraudon E. Statistical prediction of fracture parameters of concrete and implications for choice of testing standard. Cem Concr Res 2002;V. 32 (No. 4):529–56.
[34] Nana WSA, Bui TT, Limam A, et al. Experimental and numerical modelling of shear behaviour of Full-scale RC slabs under concentrated loads. Structures 2017;V. 10: 96–116.
[35] Genikomsou AS, Polak MA. Finite element analysis of punching shear of concrete slabs using damaged plasticity model in ABAQUS. Eng Struct 2015;V. 98:38–48. https://doi.org/10.1016/j.engstruct.2015.04.016.
[36] Mander JB, Priestley MJN, and, Park R. Theoretical stress-strain model for confined concrete. J Struct Eng 1988;V. 114(No. 8):1804–26.
[37] Palmquist SM, Jansen DC. Postpeak strain-stress relationship for concrete in compression. ACI Mater J 2001;V. 98(No. 3):213–9.
[38] Watanabe K, Niwa J, Yokota H, et al. Experimental study on stress-strain curve of concrete considering localized failure in compression. J Adv Concr Technol 2004; V. 2(No. 3):395–407.
[39] Tung ND, Tue NV. Post-peak behavior of concrete specimens undergoing deformation localization in uniaxial compression. Constr Build Mater 2015;V. 99: 109–17.
[40] Chang G.A., and Mander, J.B. Seismic energy based fatigue damage analysis of bridge columns: Part I - Evaluation of seismic capacity. Technical Report NCEER-94–0006, New York, 1994.
[41] Tsai WT. Uniaxial compressional stress-strain relation of concrete. J Struct Eng 1988;V. 114(No. 9):2133–6.
[42] Massone LM, Wallace JW. Load-deformation responses of slender reinforced concrete walls. ACI Struct J 2004;V. 101(No. 1):103–13.
[43] Raffoul S, Garcia R, Pilakoutas K, et al. Optimisation of rubberised concrete with high rubber content: an experimental investigation. Constr Build Mater 2016;V. 124:391–404.

[44] Bompa DV, Elghazouli AY, Xu B, et al. Experimental assessment and constitutive modelling of rubberised concrete materials. Constr Build Mater 2017;V. 137: 246–60.
[45] Raffoul S, Escolano-Margarit D, Garcia R, et al. Constitutive model for rubberized concrete passively confined with FRP laminates. J Compos Constr 2019;V. 23(No. 6):04019044.
[46] FEMA, ASCE. Prestandard and Commentary on the Seismic Rehabilitation of Buildings. Report No. 356. Federal Emergency Management Agency; 2000.
[47] Papastergiou, P. A confinement model for concrete wrapped or pretensioned with FRP. PhD thesis, Dept. of Civil and Structural Engineering, The University of Sheffield, 2010.
[48] El Khouri I., Garcia R., Taranu N., Petru M., Toma I.O., Budescu M. et al. Shake Table Tests on Frames Made with Normal and FRP-Confined Rubberised Concrete. Proceedings of the 16th European Conference on Earthquake Engineering (16ECEE). Thessaloniki, Greece, 18 - 21 June, 2018.